2017

Analysis of Micromixers on Reverse Osmosis Based Desalination Membranes

Mustafa USTA
Lehigh University

Analysis of Micromixers on Reverse Osmosis Based Desalination Membranes

By

Mustafa USTA

A Thesis

Presented to the Graduate and Research Committee

of Lehigh University

in Candidacy for the Degree of

Master of Science

in

Mechanical Engineering

Lehigh University

January, 2017

Copyright page

This thesis is accepted and approved in partial fulfillment of the requirements for the Master of Science.

_____
Date

_____
Dr. Alparslan Oztekin, Thesis Advisor

_____
Dr. Gary Harlow, Chairperson
Mechanical Engineering and Mechanics

Acknowledgements

This thesis would not have been completed without the help, motivation and advice of many individuals. First and foremost, I would like to thank my adviser, Professor Alparslan Oztekin, for his encouragement and guidance during my studies. His exceptional methodology to teach led me to reach this level.

I would like to extend my special thanks to my colleague Dr. Ali Anqi for providing me lots of valuable information about this topic.

I would also like to thank National Defense Ministry of Turkey for their financial support through Graduate Scholarship program.

I feel deep appreciation for the love, and support of my wife, Merve Usta and my dear parents help me overcome the difficulties.

Table of Contents

Abstract 1

Nomenclatures 2

1. Introduction 4

2. Theory 8

2.1. Turbulence Modelling 9

2.2. Membrane Modelling 11

3. Numerical Model 14

3.1. Computational Domain and Grid 14

3.2. The Boundary Conditions 16

3.3. Mesh Study and Validation 17

4. Results and Discussion 24

5. Conclusion 38

References 40

Vita 45

List of Figures

Figure 1. Schematic of the flow domain. 15

Figure 2. Prism mesh around a rib group for 45 million mesh elements at a random cross-section 16

Figure 3. Locations of mesh profiling for the stream-wise component of the velocity at the center (black) and concentration at the membrane surface (red) 19

Figure 4. Profile of the normalized stream-wise component of the velocity (a) and concentration (b) at $Re = 1000$ calculated using four mesh sizes along locations showed in Fig 4. 20

Figure 5. Contours of the normalized concentration at the top membrane surface. Reynolds number is set to 600 as in the experimental study 23

Figure 6. Contours of the stream-wise component of the velocity for square ribs (left column) and triangular ribs (right column). The normalized velocity contours are acquired at $Re = 100$ (a, d), $Re = 400$ (b, e) and $Re = 1000$ (c, f). 25

Figure 7. Contours of the span-wise component of the velocity for square ribs (left column) and triangular ribs (right column). The normalized velocity contours are acquired at $Re = 100$ (a, d), $Re = 400$ (b, e) and $Re = 1000$ (c, f). 26

Figure 8. Contours of the x-component of the vorticity for square ribs (left column) and triangular ribs (right column). The normalized vorticity contours are acquired at $Re = 100$ (a, d), $Re = 400$ (b, e) and $Re = 1000$ (c, f). 28

Figure 9. Contours of the vorticity for square ribs (left column) and triangular ribs (right column) at $Re = 1000$. The normalized vorticity contours are acquired for x-

component of the vorticity (a, d), y-component of the vorticity (b, e) and z-component of the vorticity (c, f). 29

Figure 10. Contours of the water flux through the top membrane for square ribs (left column) and triangular ribs (right column). The normalized water flux contours are acquired at $Re = 100$ (a, d), $Re = 400$ (b, e) and $Re = 1000$ (c, f). 30

Figure 11. Contours of the concentration along the top membrane surface for square ribs (left column) and triangular ribs (right column). The normalized concentration contours are acquired at $Re = 100$ (a, d), $Re = 400$ (b, e) and $Re = 1000$ (c, f). 31

Figure 12. Contours of the concentration along the top membrane surface for empty channel. The normalized concentration contours are acquired at $Re = 100$ (a), $Re = 400$ (b) and $Re = 1000$ (c). 33

Figure 13. Contours of the local Sherwood number (Sh) along the top membrane surface for square ribs (left column) and triangular ribs (right column). The normalized local Sh contours are acquired at $Re = 100$ (a, d), $Re = 400$ (b, e) and $Re = 1000$ (c, f). 34

Figure 14. Contours of the wall shear stress (τ) along the top membrane surface for square ribs (left column) and triangular ribs (right column). The wall shear stress is normalized by maximum values acquired at $Re = 100$ (a, d), $Re = 400$ (b, e) and $Re = 1000$ (c, f). 35

Abstract

Corrugated membranes are used in desalination modules to improve membrane performance. In this study, in order to gain a deeper insight into the separation performance of these corrugated membranes, a computational fluid dynamics simulation was carried out for a proposed three-dimensional desalination modules containing triangular and square ribs attached to the membrane surface. Solution-diffusion membrane transport model, based on coupling water permeation rate with local salt concentration, was applied for membrane boundary condition involving selective removal of components in the feed channel. The local water flux, salt concentration, shear stress, and Sherwood number were monitored over the membrane surface to determine the effect of eddy promoter corrugations on high salt concentration mitigation and total water flux for Reynolds number of 100, 400 and 1000. Mathematical model and numerical methods employed are validated by comparing predictions against measurements reported earlier. The results show that corrugated membranes especially triangular chevrons enhance membrane performance profoundly at all flow rates. Water permeation rate is increased, concentration polarization is alleviated, and the potential fouling in the module is reduced by introducing corrugated membranes. Membrane performance enhancement is greater at higher flow rate.

Nomenclatures

a_1	SST k-ω turbulent model parameters
A	Membrane permeability $[m/s\ Pa]$
c	Concentration $[kg/m^3]$
c_0	Inlet concentration $[kg/m\text{^}3]$
c_b	Bulk concentration $[kg/m\text{^}3]$
c_p	Production side membrane concentration $[kg/m\text{^}3]$
c_w	Feed side membrane concentration $[kg/m\text{^}3]$
CP	Coefficient of performance
D	Diffusion coefficient $[m^2/s]$
f	Pressure coefficient
F_1, F_2	Blending functions
h	Height of the channel
h_m	Mass transfer coefficient $[m/s]$
k	Turbulent kinetic energy $[J/kg]$
Δp	Transmembrane pressure difference $[Pa]$
Re	Reynolds number
Sc	Schmidt number
Sh	Sherwood number
$\vec{u}_i\ (u, v, w)$	Velocity vector $[m/s]$
U_{ave}	Average inlet velocity $[m/s]$
v_w	Local water flux $[m/s]$
$\vec{x}_i\ (x, y, z)$	Position vector $[m]$

Greek letters

β, β^*	SST k-ω turbulent model parameters
γ	SST k-ω turbulent model parameters
κ	Osmotic coefficient $[kPa\ m^3/kg]$
μ	Dynamic viscosity $[Pa\ s]$
μ_t	Eddy viscosity $[Pa\ s]$
ν	Kinematic viscosity $[m^2/s]$
ν_t	Kinematic eddy viscosity $[m^2/s]$
ω	Specific dissipation rate $[1/s]$
$\Delta\pi$	Osmatic pressure $[Pa]$
ρ	Density $[kg/m^3]$
σ_{k1}	SST k-ω turbulent model parameters
$\sigma_\omega, \sigma_{\omega 2}$	SST k-ω turbulent model parameters
τ_w	Normalized wall shear stress

Subscripts

i and j	Index notation
w	Properties along the membrane surface

1. Introduction

Reverse Osmosis (RO) desalination has gained attention worldwide to produce freshwater. This process depends on reversing the osmotic phenomenon. Seawater or brackish water is pumped through a channel of semi-permeable membranes. Pure water passes through membranes if the flow pressure exceeds the osmotic pressure of the solution. Spiral wound membrane is based on this principle and used widely in water desalination [1,2]. In spiral wound module, a net of spacers are placed between two-membrane leaves to form the feed channel. The spacers maintain a gap between the membranes and promote turbulence in the feed channel. However, the presence of spacers increases the pressure drops in the feed channel, and the fresh water production cost goes higher as the pressure drop increases [3]. Nowadays, membranes have become highly water-permeable and very salt-selective. Such membrane's properties cause strong salt concentration polarization near the membrane surface, and fouling has a great chance to occur at the membrane surface. Belfort at al. [4] have reported that the concentration polarization and fouling can be mitigated chemically, hydrodynamically and/or physically.

Several investigators [5–17] have studied the flow with or without mass transfer in the feed channel. Koutsou and his team [13,14] conducted experimental and direct numerical simulations of the flow and mass transfer. Their study concluded that high values of mass transfer coefficient and low fouling regions coincide with areas of high wall shear stress along the membrane surface. Neal et al. [15] studied experimentally particle deposition in spacer-filled channels. The experiment proved a direct relation between

particle deposition behavior and spacer geometry. Turbulent flow helps to alleviate the salt concentration polarization near the membrane surface. The reduction of salt concentration reduces the osmotic pressure in the vicinity of the membrane in the feed side, and, therefore, the pure water production improves. Mahdavifar et al. [16] employed direct numerical simulations to study the flow in channel with spacers. These investigators concluded that, by placing the spacers in a channel, the flow becomes turbulent at low Reynolds number when compared to the flow inside an empty channel. Kang and Chang [17] performed numerical simulation and experimental flow visualization to study the flow and mass transfer in a channel with ribs attached to membranes in different configurations. They observed that the flow transition from laminar to turbulent regime occurs at Reynolds number above 300; Reynolds number is based on the channel height and the average bulk velocity. They reported that the mass transfer coefficient was enhanced considerably when ribs were attached to membranes. As mentioned above, the spacer insertion increases the pressure drop in the feed channel, and another way to boost the membrane performance is needed.

In the last two decades, several researchers [18–23] have fabricated membranes with patterns on the membrane surface to eliminate the usage of spacers. Scott et al. [18] modified commercial membrane by via mechanical pressing to form a corrugated membrane. The corrugated membrane was then used to filter water-in-oil emulsion. Scott and his coworkers reported up to 160% increase of the flux through the membrane and up to 88% of energy savings when compared to a plane channel with flat membranes. Another membrane alteration was done by Maruf and his team [19,20]. They used Silicon (Si) mold

with sub-micron patterns to imprint the patterns on an ultrafiltration membrane surface [19] and on a thin film composite membrane for reverse osmosis [20]. These studies concluded that the membranes with patterns became more fouling resistant than the flat membranes. Kharraz et al. [21] fabricated a polyvinylidenfluoride (PVDF) corrugated membranes for water distillation and performed experimental testing and surface characterization. Kharraz et al. documented that the corrugated membranes maintained better water flux level and antifouling than the flat membranes. Maruf et al. [19,20] and Kharraz et al. [21] anticipated that the patterns on the membrane surface promote more mass and momentum mixing which enhances the membrane performance. Ho et al. [22] and Altman et al. [23] have studied numerically and experimentally the water desalination by reverse osmosis membranes with three-dimensional (3D) printed patterns. The patterns were created by a 3D printer using UV-curable epoxy, and the patterns were laid on the RO membrane a chevron-like shape in different configurations. The numerical simulations in [22,23] considered the flow in the feed channel without the mass transfer. The patterns on the membrane caused a chaotic flow in the feed channel [22]. The membrane with patterns had less biofouling than the membrane with spacers, but the membrane with spacers had more water flux [23].

The present work conducts computational fluid dynamics simulations to characterize flow structures in channels containing in-phase chevrons on both top and bottom membrane and to predict concentration field to assess the effect of corrugation on the membrane flux performance, the shear stress and the concentration polarization characteristics. The laminar flow model is employed for Reynolds number of 100, while

k-ω Shear Stress Transport (SST) turbulence model is used for Reynolds number of 400 and 1000. The solution-diffusion model based membrane flux model is applied and the water permeate loss is taken into account to mimic real membrane module operating conditions.

2. Theory

The dynamics of fluid flows are modeled using equations based on conservation of mass and momentum. Conservation of mass for incompressible fluids yield

$$\frac{\partial u_i}{\partial x_i} = 0 \tag{1}$$

Conservation of momentum with augmentation of a Newtonian law of viscosity produce Navier-Stokes (NS) equations governing fluids motions. For steady flows with constant physical properties NS equations reduce to the following form:

$$u_j \frac{\partial u_i}{\partial x_j} = \frac{1}{\rho}\frac{\partial p}{\partial x_i} + \nu \frac{\partial^2 u_i}{\partial x_j \partial x_j} . \tag{2}$$

Mass transport equation governs the concentration field. It can be written in the following form:

$$u_j \frac{\partial C}{\partial x_j} = D \frac{\partial^2 C}{\partial x_j \partial x_j} \tag{3}$$

Here i and j are the summation indices. $x_1 = x$ is the stream-wise direction, $x_2 = y$ is the cross-flow direction, and $x_3 = z$ is the span-wise direction. $u_1 = u$ is the stream-wise component, $u_2 = v$ is the cross-flow component, and $u_3 = w$ is the span-wise component of the velocity. In equation (2) ρ is density, ν is kinematic viscosity and p is pressure of the binary solution which is assumed to be incompressible. In equation (3), D is diffusion coefficient and C is the concentration of salt. The fluid considered is the binary mixture of salt and water.

2.1. Turbulence Modelling

Most of the fluid flow systems encountered in the engineering applications are characterized in fully or transition to turbulent flow regime. It is documented in several studies [16,24] that low level of turbulence were observed for $Re < 1000$ in complicated flow systems involving flow separations. Tamburini et al. [24] was carried out Direct Numerical Simulations (DNS) for bulk Reynolds number Re about 600 in a feed channel containing spacers in different arrangements. They reported that the DNS predictions reveal strong sign of turbulent fluctuations likewise the calculated value of velocity power spectra in the time-frequency domain strengthen their findings.

As our intention is coupling the suction rate and local concentration over the membrane surface, resolving the boundary layer have significant impact on flux model accuracy mainly for this elevated Schmidt number. On the basis of aforementioned points, well-documented SST k-ω turbulence model [25] using the standard k-ω model and a transformed k-ε model, is employed to predict steady-state flow and concentration field accurately. Major contribution of SST k-ω model relies on its methodology for treating inner boundary layer and wake region with different models with the help of blending function F_1. It activates the k-ω model in the near wall region and the k-ε model for the rest of the flow. By this approach the attractive near-wall performance of the k-ω model can be used without the potential errors resulting from the free stream sensitivity of that model. In addition, the SST model also features a modification of the definition of the eddy viscosity, c_μ, which is treated as a variable. On the other hand, c_μ in the k-ε model is taken as a constant. This modification is required to accurately capture the onset of separation

under pressure gradients. A production limiter is used in the SST model to prevent the build-up of turbulence in stagnation regions. The SST k-ω model can be expressed from [25] as

$$u_j \frac{\partial u_i}{\partial x_j} = -\frac{1}{\rho}\frac{\partial p}{\partial x_i} + \frac{1}{\rho}\frac{\partial}{\partial x_j}\left((\mu + \mu_t)\frac{\partial u_i}{\partial x_j}\right) \quad (4)$$

where $\mu_t = \rho \frac{a_1 k}{max(a_1\omega; \Omega F_2)}$ is the eddy viscosity. The equation governing k and ω for SST k-ω turbulence model are as follows

$$u_j \frac{\partial(\rho k)}{\partial x_j} = \tau_{ij}\frac{\partial u_i}{\partial x_j} - \beta^*\rho\omega k + \frac{\partial}{\partial x_j}\left[(\mu + \sigma_{k1}\mu_t)\frac{\partial k}{\partial x_j}\right] \quad (5)$$

$$u_j \frac{\partial(\rho\omega)}{\partial x_j} = \frac{\gamma}{\nu_t}\tau_{ij}\frac{\partial u_i}{\partial x_j} - \beta\rho\omega^2 + \frac{\partial}{\partial x_j}\left[(\mu + \sigma_\omega\mu_t)\frac{\partial \omega}{\partial x_j}\right] + 2\rho(1 - F_1)\sigma_{\omega 2}\frac{1}{\omega}\frac{\partial k}{\partial x_j}\frac{\partial \omega}{\partial x_j} \quad (6)$$

Here, k and ω are the turbulent kinetic energy and the specific dissipation rate, respectively, Ω is the vorticity magnitude, $a, a_1, \beta, \beta^*, \sigma_k, \sigma_\omega, \sigma_{\omega_2}$ are closure coefficients, and F_1 is the blending function.

Species equation for the k-ω SST model is of the form:

$$u_j \frac{\partial C}{\partial x_j} = \frac{\partial}{\partial x_j}\left((D + D_T)\frac{\partial C}{\partial x_j}\right) \quad (7)$$

$D_T = \frac{\mu_T}{\rho Sc_T}$ is the eddy diffusion coefficient and Sc_T is the turbulent Schmidt number. The turbulent Schmidt number is selected to be 0.85 in the present work while Schmidt number for flow is set to 667.

2.2. Membrane Modelling

Along with the developments on membrane technologies, researchers have devoted their efforts to understand fundamental mechanism of membrane separations and develop mathematical models. Some of the proposed models were approached with simple concepts, while others were relied on sophisticated transport phenomena that can be categorized in three main groups: (1) irreversible thermodynamics models (such as Kedem-Katchalsky and Spiegler-Kedem models), (2) pore models (such as finely-porous and surface force-pore flow models) and (3) nonporous or homogeneous membrane models (such as solution-diffusion model) [26].

As one of the early developed models, irreversible thermodynamics treats the membrane as a "black box" and introduces a correlation between transport and mechanical/osmotic pressure gradients [27]. These models assume that slow processes proceed near equilibrium in small divided sub-systems which led to derivation of flux using phenomenological thermodynamics relationships. Kargol et el. [28] reported that this model's prediction of flux for high concentration deviation across the membrane circumstances is not accurate due to near equilibrium assumption.

Porous models take straight cylindrical physical pores across the membrane layer into account and describes the separation mechanism by surface phenomena and fluid transport through pores. The model proposed by Okada and Matsuura [29], introduce two more assumptions: (1) there is a continuous gradient of chemical potential, and (2) chemical potential gradient across the membrane can be expressed as a pressure gradient. Sukitpaneenit et al. [30] experimentally and theoretically employed classical pore-flow

model and introduced a modified pore-flow model which differs by factoring in the contribution of Knudsen flow to vapor transport. They noted that transport parameters are strongly dependent on the membrane pore size and the solvent in contact. The porous model exhibits an accurate estimation for the mass transport.

On the contrary to porous models, homogeneous or solution-diffusion models consider that the membrane is "nonporous" medium as a primary assumption. The model was proposed by Lonsdale et al. [31] and derivation of solution-diffusion model using a chemical potential was illustrated by Wijmans and Baker [1]. They have reported that diffusion of the solute and solvent by their own chemical potential gradient, which are the results of concentration and pressure gradient across the membrane, is a proper approach to determine flux of species independently. Additionally, when the solution-diffusion model is compared to most of other transport models, the model becomes prominent as it also takes into account the rate at which the solute or solvent partition into the polymeric membrane of interest [27]. In order to take abovementioned advantages, the solution-diffusion model was employed in the present study. In the numerical model membrane surfaces are treated as a functional surface where the local water flux, the local salt concentration and the local pressure gradient across the membrane are coupled and solved simultaneously. As membrane is considered to be nonporous, no slip wall boundary condition applies to the membrane surfaces while local water flux and the local salt concentration equations at the membrane surfaces defined as:

$$\left.\begin{aligned} v_w &= A[\Delta p - \Delta\pi] \\ D\frac{\partial C}{\partial y} &= v_w(C_w - C_p) \end{aligned}\right\}, \Delta\pi = \boldsymbol{\kappa}\left(C_w - C_p\right) \tag{8}$$

Here v_w is the local water flux through the membrane, D is the diffusion coefficient of the water-salt solution, Δp is the transmembrane pressure difference, C_w is the local salt concentration at the membrane surface, A is the water permeability through the membrane, $\boldsymbol{\kappa}$ is the osmotic pressure coefficient, $\Delta\pi$ is the osmotic pressure and C_p is the salt concentration in the production side. It should be noted that with the assumption of ideal salt rejection, permeate side salt concentration C_p is set to $0\ ppm$.

3. Numerical Model

Over the course of many years, CFD packages has taken its place more intensely in the engineering applications by the side of experimental techniques. Their increased capabilities of solving flow equations with finer resolution, enabled to estimate complicated flow behavior more accurately. In light of these developments, the present study employs a commercial CFD package ANSYS-CFX 14.5 for modelling of flow field, mass transfer and pressure driven membrane process.

3.1. Computational Domain and Grid

Figure 1 illustrates the broken view of the geometry containing groups of ribs on the surface of the wound membrane. Ribs are designed in two different geometry as square and triangular cross-sections while square one is depicted in the Fig. 1. The base and height of the ribs for both geometry are set to $0.2h$, where h is the gap between two parallel spiral wound membrane. The feed channel contains 8 groups of ribs along the flow direction with the spacing of $5h$ and the spacing between two consecutive rib in each 3 ribbed group is $1.1h$. The length and width of the channel is assigned as $50h$ and $10h$, respectively. Specific surfaces of the computational domain are indicated in Fig. 1.

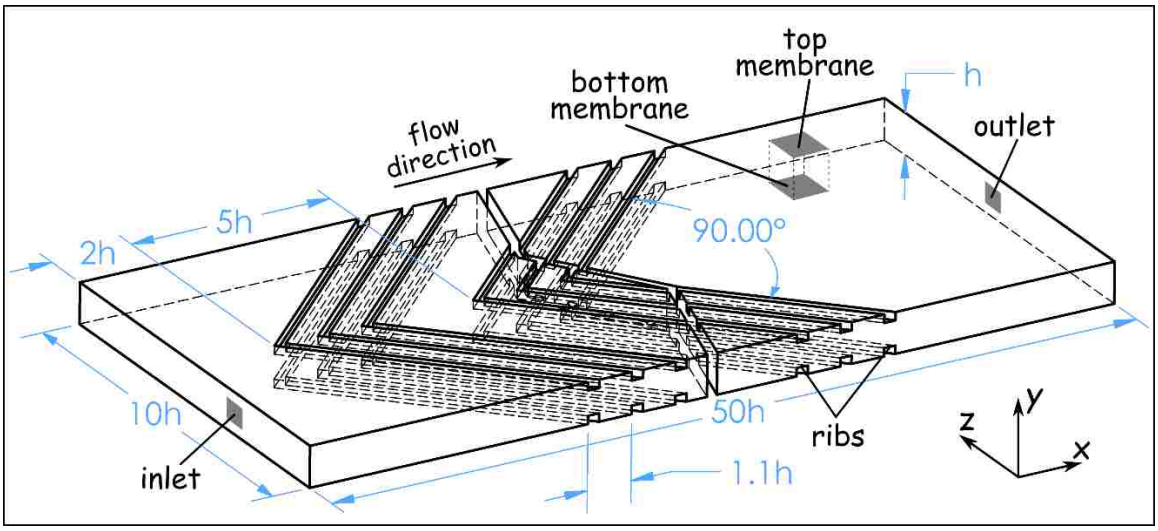

Figure 1. Schematic of the flow domain.

SolidWorks is used to generate three dimensional geometries and ANSYS-CFX 14.5 Mesh tool is used to mesh the geometry and to perform the mesh analysis. Figure 2 depicts a prism mesh view around a triangular rib group for 45 million mesh elements at randomly selected cross-section. As seen in the Fig. 2 local mesh refinements were applied to vicinity of sharp edges and inflation layers, which are maintaining thin enough thickness of the first grid element layer ($< 3\mu$, order of 1% of the rib height), were inserted to predict quickly developing concentration boundary layer.

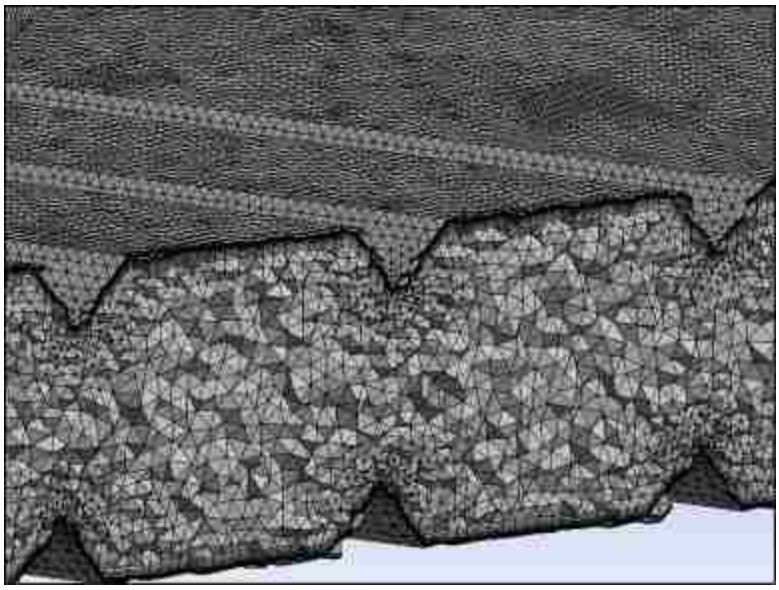

Figure 2. Prism mesh around a rib group for 45 million mesh elements at a random cross-section

3.2. The Boundary Conditions

Obtaining solutions to set of coupled transport equations requires assigning appropriate boundary conditions. In this sub-chapter, the boundary conditions of the 3D domain will be specified.

For our proposed work assigning a boundary condition for membrane surfaces plays a key role for accurate estimation of overall performance of the membrane module. As explained in membrane modeling section, the solution-diffusion model, which defines the water permeation rate in terms of local salt concentration and pressure, is employed due to its advantages such as coupling of local water flux, local salt concentration and pressure. In the model, top and bottom walls are considered as functional surface and permeable wall to represent the actual membrane surface. The operating physical parameters of the solution-diffusion model are listed in Table 1.

Table 1. Physical parameters used in the simulations.

Parameter	Value
Concentration in production side: c_p	$0\ ppm$
Density: ρ	$1000\ kg/m^3$
Dynamic viscosity: μ	$10^{-3}\ Pa\ s$
Diffusivity: D	$1.5 \times 10^{-9}\ m^2/s$
Osmotic pressure coefficient: κ	$75\ kPa\ m^3/kg$
Permeability: A	$2.3 \times 10^{-11}\ m/(s\ Pa)$
Schmidt number: Sc	667
Transmembrane pressure Δp	$1.25\ MPa$

Uniform velocity and uniform concentration profile are used at the inlet where constant concentration of $c_0 = 4000\ ppm$ is specified. At the outlet, constant pressure and constant gradient boundary conditions are applied. For side walls, periodic boundary conditions are selected on both velocity and concentration fields to represent the practical reverse osmosis module configuration where membrane sheets are wider.

3.3. Mesh Study and Validation

In this study CFD simulations were conducted for a rectangular cross-sectioned feed channel containing groups of ribs arranged in-phase. Results are presented for Reynolds numbers of 100, 400 and 1000. Reynolds number is defined based on the channel height and the inlet velocity as $Re = U_{ave}h/\nu$. To predict steady-state velocity and concentration fields, laminar flow model was used for $Re = 100$ while SST k-ω turbulence model was used for $Re = 400$ and 1000. The physical properties of the

brackish water in the computational domain are considered to be constant. The density is $\rho = 1000\ kg/m^3$ and the dynamic viscosity is $\mu = 10^{-3}\ Pa\ s$.

When utilizing numerical approaches such as finite volume method to solve set of transport equations, which are in the form of partial differential equations, numerical errors can be produced from various sources. These potential errors have to be addressed to get an accurate solution for intended computational domain bounded with specific boundary conditions. While there are several parameters, average residue appears as to be the first criteria to check convergence of solution. In the present study, average residue is aimed to be lower than 1E-08 level to accept the solution as converged. However, this not the only step before one can obtain reliable results. A grid independence study was also performed to estimate the amount of error associated with the grid. Considering to generate an optimum mesh, it was decided to monitor profiles of the stream-wise component of the normalized velocity for the bulk flow and profiles of the normalized concentration on the membrane surface at $Re = 1000$ for triangular rib case.

Figure 3 shows lines along the feed channel where profiles of both velocity and concentration are obtained. The lines are located $2.5h$ away from the closest side wall. The red line (on the membrane surface) is for concentration and the black line (at the center of cross-flow direction) is for velocity. It is intended to study the grid convergence of velocity field in bulk flow while concentration along the surface. Because it is well documented by many researchers that prediction of the local salt concentration on the membrane surface is essential step toward an accurate membrane flux model.

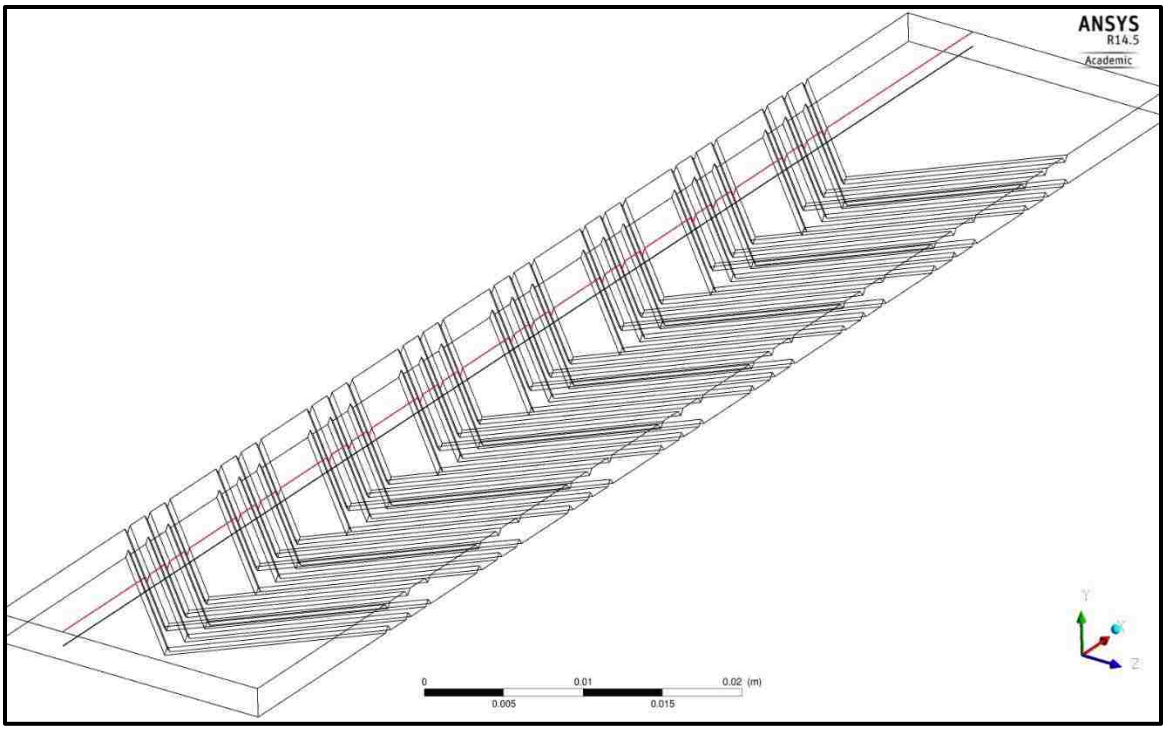

Figure 3. Locations of mesh profiling for the stream-wise component of the velocity at the center (black) and concentration at the membrane surface (red)

As the current study intends to exhibit the results for steady-state simulations, only spatial convergence test is required. The mesh study is performed for four different mesh density: 24 million elements, 32 million elements, 45 million elements, and 52 million elements. Figure 4a shows the profiles of stream-wise component of normalized velocity (u/U_{ave}) as a function of the stream-wise direction (along the black line shown in Fig.3). The profiles of normalized concentration (c/c_0) along the surface of membrane (the red line shown in Fig. 3) is depicted in Fig. 4b. Velocity and concentration profiles demonstrate that good mesh convergence is obtained at the 45 million elements or more. In particular, the local salt concentration is well predicted at the downstream and upstream of the ribs.

Thus, 45 million mesh element is used in the current study to characterize the flow and concentration field and the membrane performance.

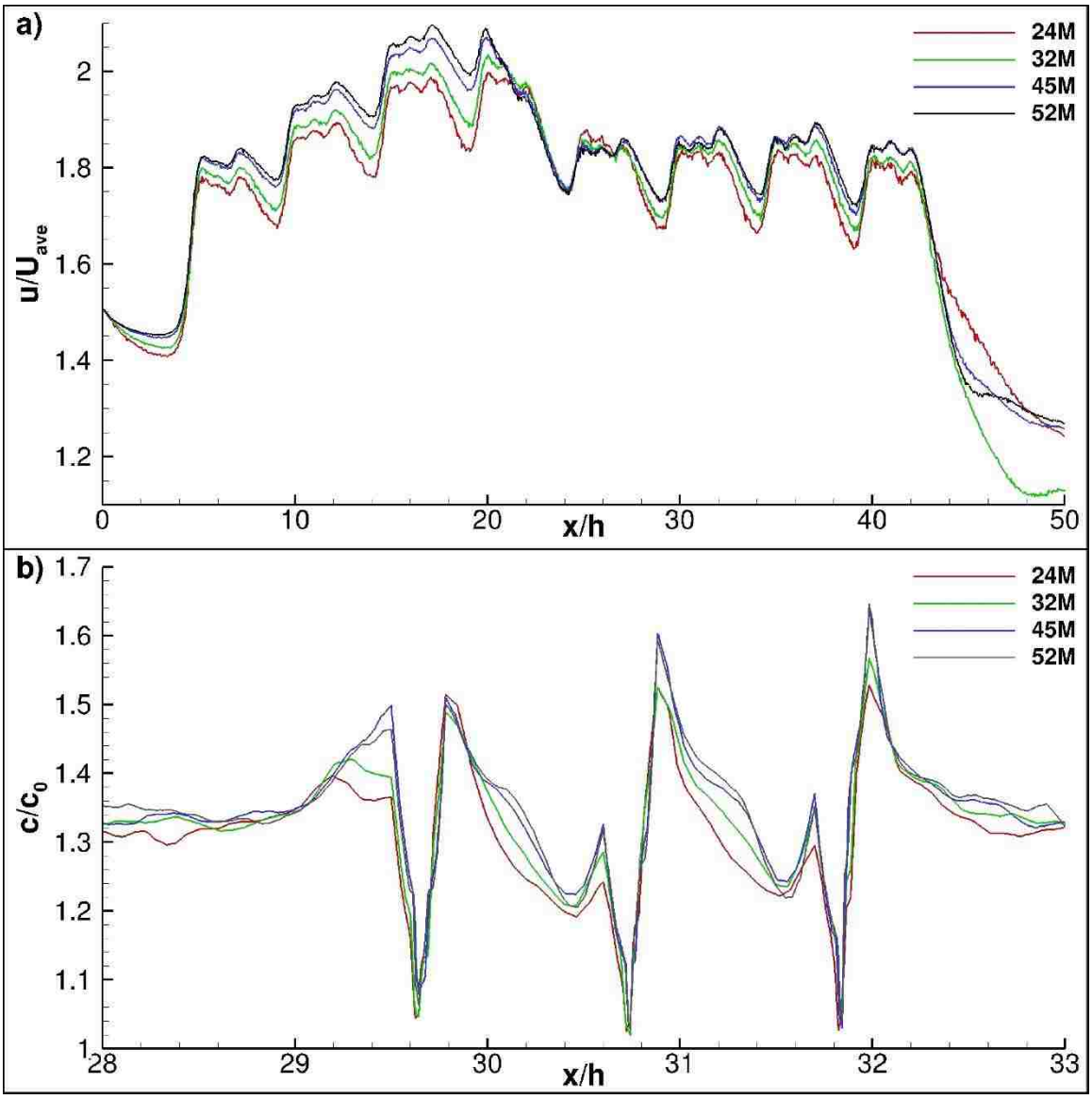

Figure 4. Profile of the normalized stream-wise component of the velocity (a) and concentration (b) at $Re = 1000$ calculated using four mesh sizes along locations showed in Fig 4.

Beyond reducing the numerical errors, validation of computational fluid dynamics simulations is another crucial step toward an accurate estimation of intended parameters.

While solving a set of equations with proper approach assures the stability of numerical solutions, it is still deprived of validating the proposed mathematical model for problem specific. In order to validate the numerical predictions, it is preferred to compare the results with results of analytical solutions or results of experimental studies. In the case of analytical solutions or experimental measurements are lacking comparisons against well-established numerical solutions could be beneficial.

Ho et al. [22] have conducted sets of experiments with a membrane module containing 3D printed chevrons on the membrane sheet and utilized CFD techniques to obtain a solution for the same specific geometry. It is worth to mention that their numerical approach was subject to several simplifications. They have studied the effects of micromixer on performance and fouling/scaling of reverse osmosis desalination membranes for in-phase and out-of-phase chevrons with two different spacing at Reynolds number of around 600. They have reported that the resulting area averaged initial permeate fluxes per hour were 95 and 99 $L\ /\ m^2\ h$ for repeated experiments. As their study can be comparable with the current study in terms of many aspects, 10% in-phase geometry was generated for validation and proposed mathematical model consisting SST k-ω turbulence model and the solution-diffusion model applied to this geometry at same values of operating parameters. The permeate flux averaged over the module was obtained as 96.78 $L\ /\ m^2\ h$. The water permeate predicted by the present study agrees well with the measured rate of water permeation.

In addition the quantitative comparison, a qualitative comparison was made. Contours of the normalized concentration on the membrane surface is depicted in Fig. 5.

In accordance with the experimental findings, higher concentrations of salt were found at downstream of ribs, presumably because of wake flow. The behavior of concentration distribution along span-wise direction was observed as repeated bands of relatively high and low concentrations that can be attributed to mechanism of flow separation, while upstream-pointing chevrons ("peaks") are separating the flow, downstream-pointing chevrons ("valleys") merges the incoming flow. Particularly, it was also found out that high salt concentration band around downstream of valleys was separated and settled at both side of tips of downstream of valleys toward last chevrons as observed in the experimental study. To investigate the correlation between this behavior and flow speed further simulations were carried out for $Re = 400, 800$ and figured out that aforesaid separation is specific to $Re = 600$ which was the actual flow speed in the experimental studies. Good qualitative and quantitative agreements between our predictions and experimental measurements validate the mathematical model for transport in desalination module and the numerical method employed.

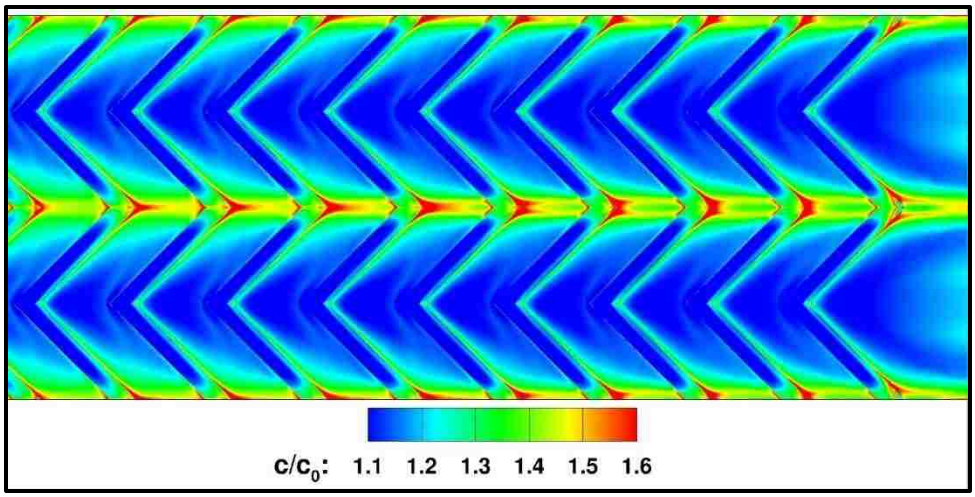

Figure 5. Contours of the normalized concentration at the top membrane surface. Reynolds number is set to 600 **as in the experimental study**

4. Results and Discussion

This part of the paper presents and discusses the results of the flow and concentration simulations of the feed channel containing ribs to examine possible mass transfer enhancements on RO desalination modules. The results are presented in some selected dimensionless quantities in addition to common flow visualization parameters such as velocity and vorticity. The friction coefficient is evaluated from:

$$f = \frac{2h \left|\frac{dp}{dx}\right|}{0.5\, \rho U_{ave}^2} \tag{9}$$

where $\left|\frac{dp}{dx}\right|$ is the pressure gradient along the stream-wise direction. Sherwood number, Sh, is evaluated by the following expression:

$$Sh = \frac{(2h)\, h_m}{D}, \quad h_m = \frac{D \left.\frac{dc}{dy}\right|_{y=h}}{(c_b - c_w)} \tag{10}$$

where h_m is the local mass transfer coefficient, c_b and c_w are bulk and wall concentration, respectively.

Figure 6 shows contours of the stream-wise component of normalized velocity at $Re = 100$, 400 and 1000 for square and triangular ribs. The contours are depicted at mid-y-plane and the values are normalized with average inlet velocity, U_{ave}. For all values of Reynolds number, it is clearly observed that presence of the ribs reduces the flow cross-section area which yields to high speed flow region. Additionally, as the square ribs tent to cause more wall friction and elevated pressure drop, the velocity in high speed region is relatively higher in the geometry with square ribs than in the geometry with triangular ribs.

In particular, higher flow speed trigger the secondary flow activities as depicted in Fig 6c. and 6f. While primary flow is dominated for $Re = 100$ and 400, contribution of secondary flows manifested by flow transitions is significant for $Re = 1000$. Three dimensional effects become more pronounced at higher flow rates. It is also observed that for all cases flow becomes hydrodynamically developed downstream as fluid passes through ribs. This is evident from the fact that repeated flow patterns are observed behind arrays of ribs in all cases.

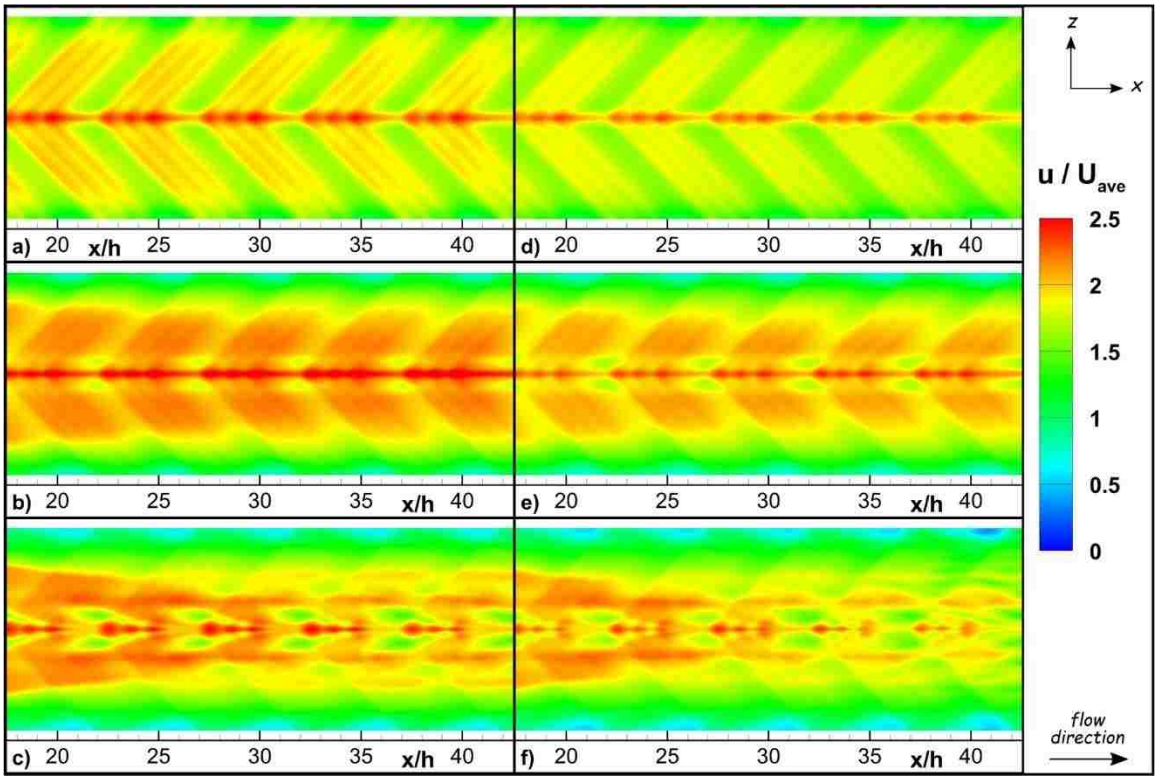

Figure 6. Contours of the stream-wise component of the velocity for square ribs (left column) and triangular ribs (right column). The normalized velocity contours are acquired at $Re = 100$ (a, d), $Re = 400$ (b, e) and $Re = 1000$ (c, f).

The contours of the span-wise component of the velocity for both rib geometry and all flow speeds are depicted in Fig. 7. The location of contours are selected to be mid-plane

in the cross-flow direction. The values are normalized with the average inlet velocity, U_{ave}. Even at low flow rate, the span-wise component of the velocity is observed to be nonzero. The flow in the span-wise direction can be induced by the presence of ribs. The cross flow in the module is more pronounce for $Re = 400$, particularly at vicinity of rib intersections. However at highest flow rate a flow transitions occurs and regions with greater span-wise component of velocity expand toward side walls. This behavior can be attributed to secondary flows manifested by flow transitions. Geometry with triangular ribs have stronger secondary flows.

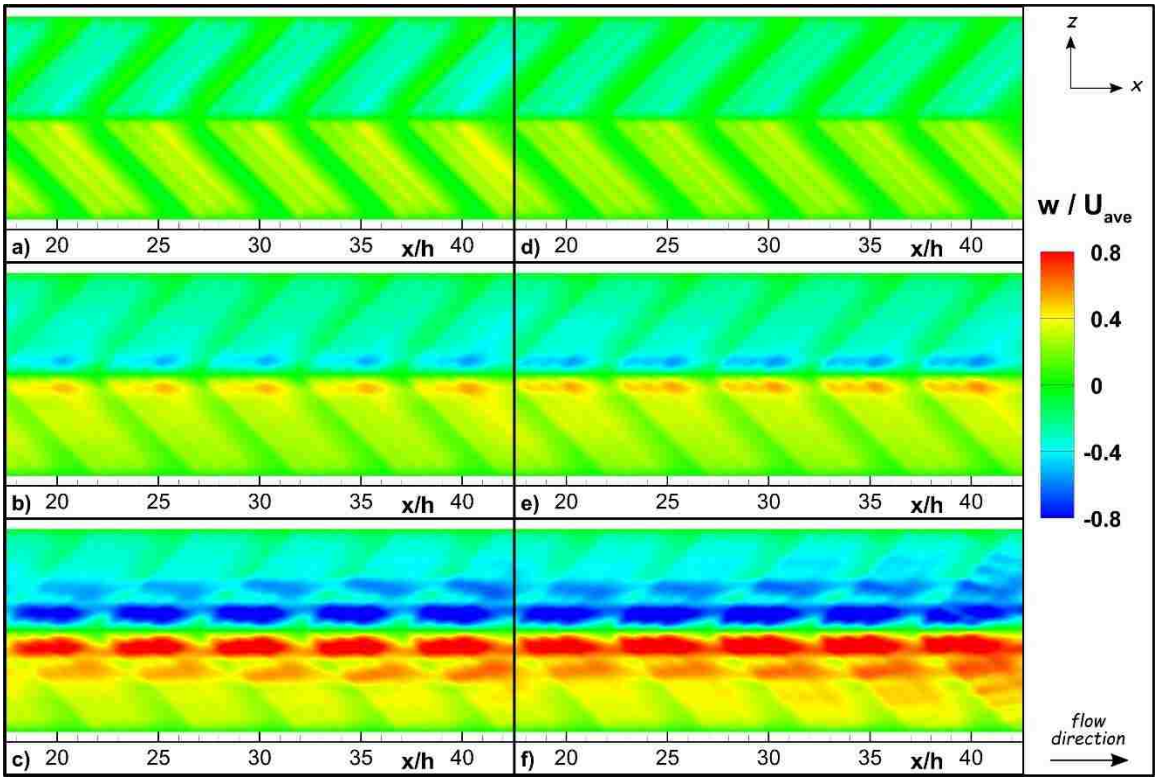

Figure 7. Contours of the span-wise component of the velocity for square ribs (left column) and triangular ribs (right column). The normalized velocity contours are acquired at $Re = 100$ (a, d), $Re = 400$ (b, e) and $Re = 1000$ (c, f).

Figure 8 illustrates contours of the stream-wise component of the vorticity for Reynolds numbers of 100, 400 and 1000 at y-plane located $0.15h$ away from the lower membrane surface. This location was selected to better capture the vortical activities induced by the presence of ribs. The vorticity is normalized by ν/h^2. Due to diagonal arrangements of the ribs, cross flow is generated for all flow rates considered. The cross flow in the module can generate vorticity in the stream-wise direction. The magnitude of the vorticity is greater at the intersection of ribs for all flow rates considered, as shown in Fig. 8. The flow structures alter significantly as flow rate is varied. Away from the intersection of the ribs, the flow is nearly uniform along the rib at $Re = 100$. As Re is increased to 400, it is observed slight variation of the flow structure along ribs. Vortices breakup and become nearly periodically spaced along the rib with decreasing intensity away from the intersection of ribs, as shown in Figure 8c and 8f. The vortical activities are slightly more intense for triangular ribs compared to those for rectangular ribs, but they demonstrate very similar flow structures. Strong secondary flows caused by ribs indicate that the mixing is greatly enhanced in the module with the addition of ribs. It is well known the flow structure greatly influence the membrane performance in a desalination module. Enhanced mixing improves membrane performance, alleviates concentration polarization and reduces potential for fouling [5,8,10,11,32,33].

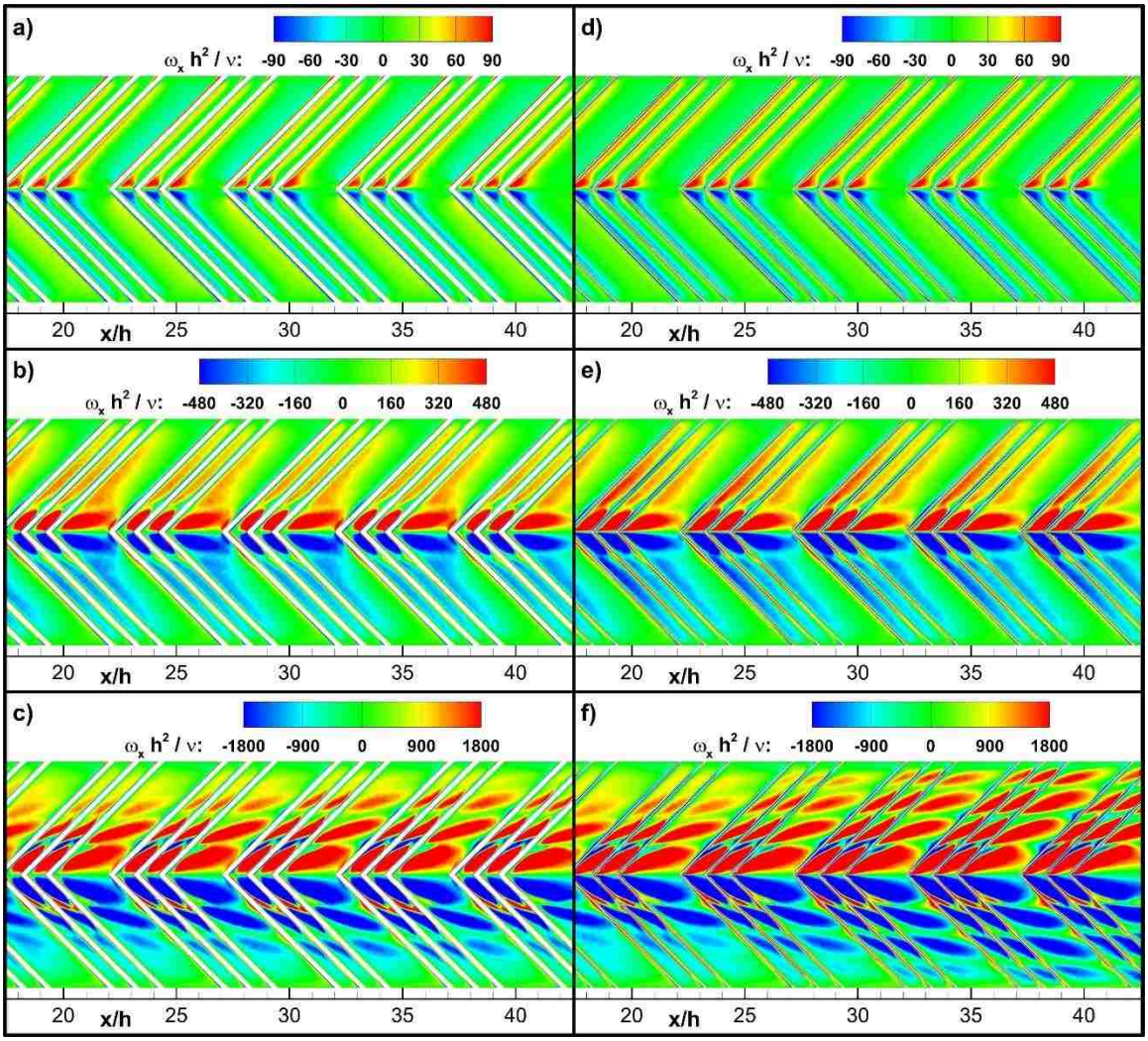

Figure 8. Contours of the x-component of the vorticity for square ribs (left column) and triangular ribs (right column). The normalized vorticity contours are acquired at $Re = 100$ (a, d), $Re = 400$ (b, e) and $Re = 1000$ (c, f).

Contours of the span-wise and crossflow components of vorticity are depicted in Fig. 9 for $Re = 1000$. Vorticity contours are acquired at the y-plane $0.15h$ away from the lower membrane. Strong presence of secondary flows are also manifested in both span-wise and crossflow components of the vorticity in both geometry. The intensity of vorticity is much greater in the region where ribs intersect and decays gradually away from that

region. There still are present strong vortical activities nearly everywhere in the domain; resulting in elevated momentum mixing in the module.

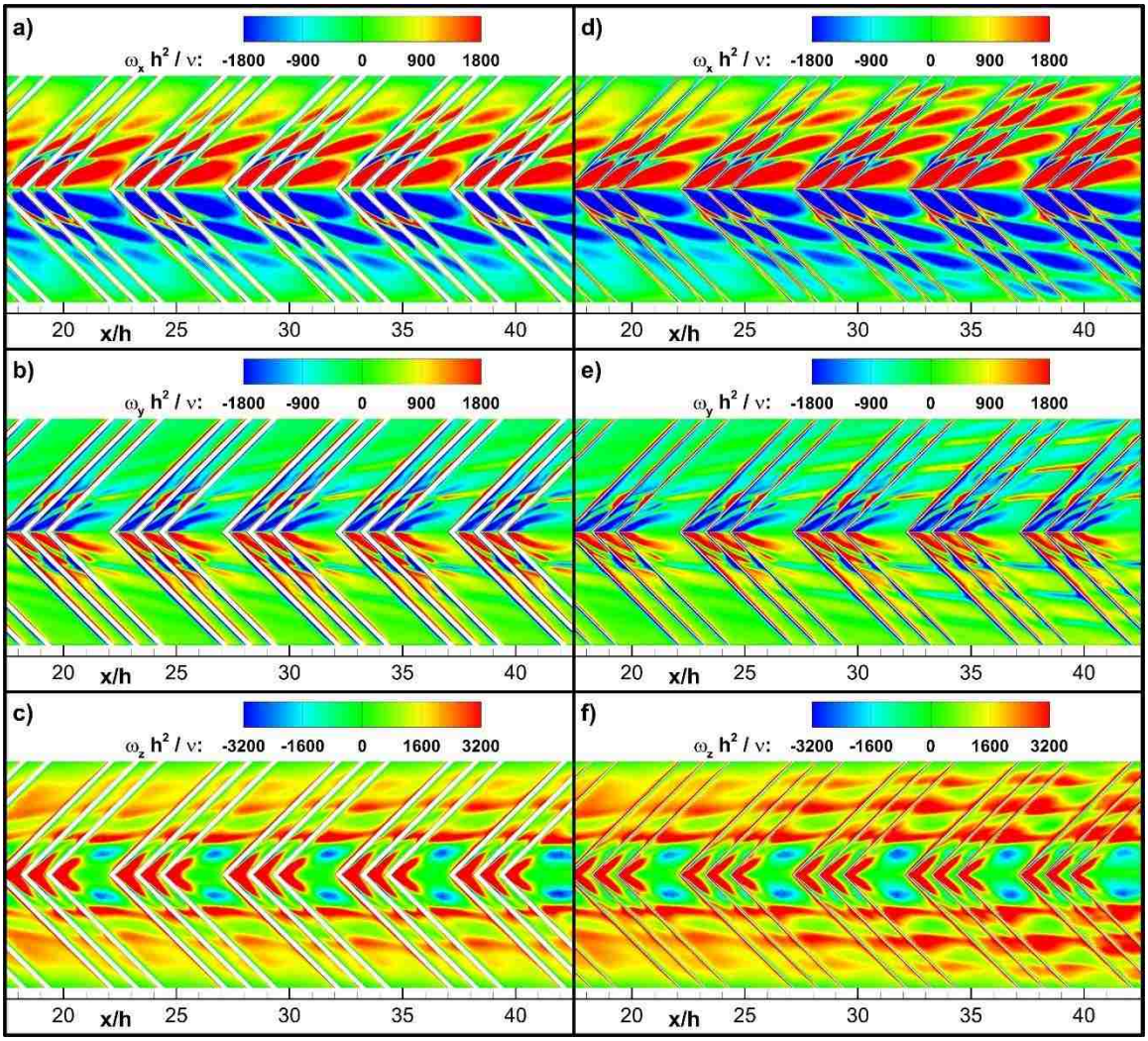

Figure 9. Contours of the vorticity for square ribs (left column) and triangular ribs (right column) at $Re = 1000$. The normalized vorticity contours are acquired for x-component of the vorticity (a, d), y-component of the vorticity (b, e) and z-component of the vorticity (c, f).

Figure 10 shows contours of the local water flux through the top membrane in desalination module with square and triangular ribs. A common legend is employed with the use of normalized quantities to indicate how suction rate is influenced by flow rate. The

water permeate increases immensely as the flow is increased, as depicted in Fig. 10. Also, it is observed that the water permeate is slightly greater in the module with triangular rib compared to that in the module with square rib at all flow rates. In the region near upstream face of the rectangular ribs lower rate of water permeate is obtained, as indicated in Fig. 10. It is also noted that spatial distribution of the water permeate in the span-wise and stream-wise direction closely follow the vorticity patterns in the module.

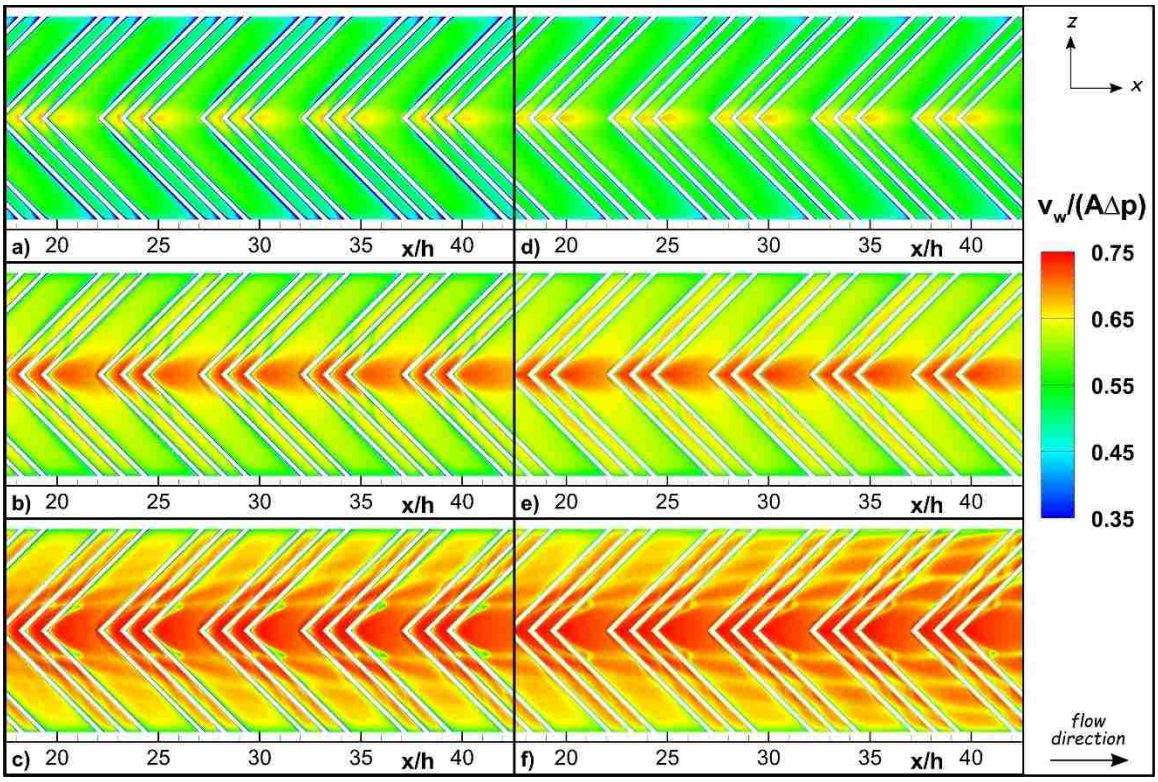

Figure 10. Contours of the water flux through the top membrane for square ribs (left column) and triangular ribs (right column). The normalized water flux contours are acquired at $Re = 100$ (a, d), $Re = 400$ (b, e) and $Re = 1000$ (c, f).

Contours of the concentration along the surface of the top membrane are illustrated in Fig. 11 for both geometry. Images on the left are acquired for the module with rectangular ribs while images on the right are acquired for the module with triangular ribs.

Images are shown for $Re = 100$ (top row), $Re = 400$ (middle row) and $Re = 1000$ (bottom row). In both geometry, regions where high water permeation occurs coincides with regions of low concentration (see Figure 10 and Figure 11). Concentration polarization is alleviated in both geometry compared to the module without ribs at all flow rates (as indicated by contours of the concentrations in the module without ribs, see Fig. 12). It is also important to note that the intensity of concentration polarization is greatly reduced as flow rate is increased in both geometry. Concentration polarization is lesser in the module with triangular ribs compared to that in the module with square ribs at all flow rates. There is a more pronounced difference at the lower flow rate, as shown in Fig. 11.

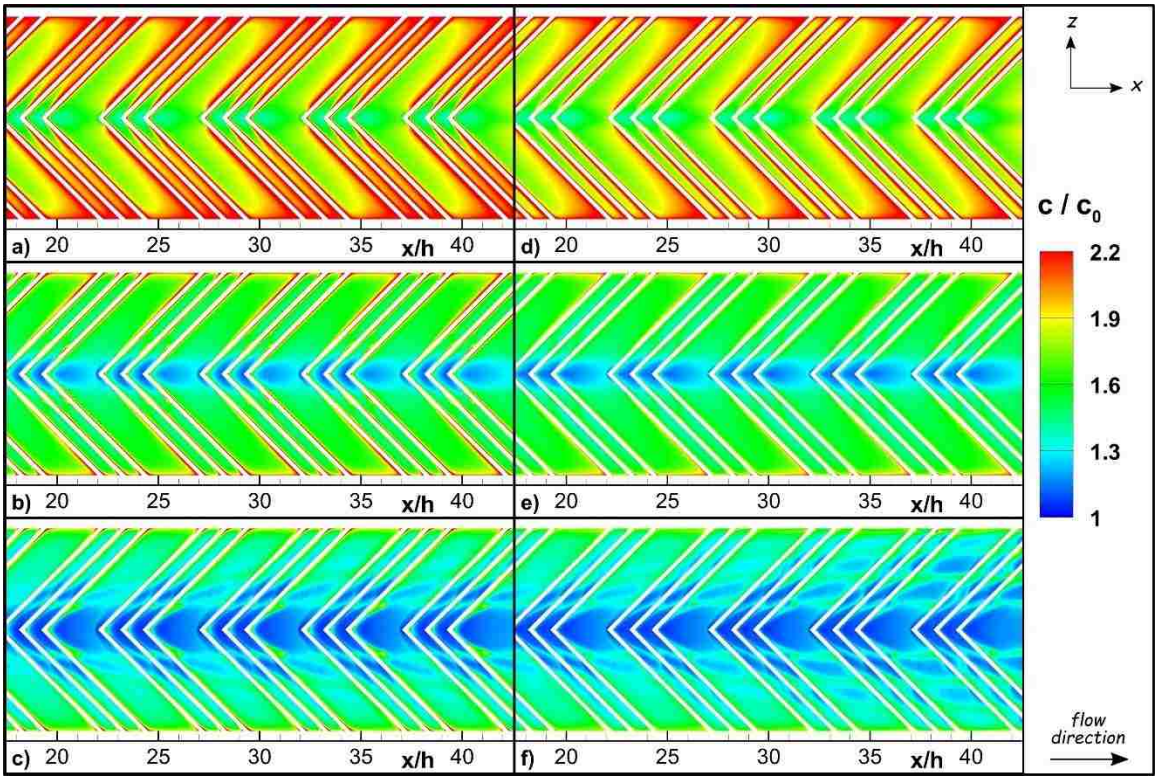

Figure 11. Contours of the concentration along the top membrane surface for square ribs (left column) and triangular ribs (right column). The normalized concentration contours are acquired at $Re = 100$ (a, d), $Re = 400$ (b, e) and $Re = 1000$ (c, f).

Figure 12 shows contours of the concentration along the top membrane surface for the geometry without the ribs for $Re = 100,\ 400$ and 1000. Basically these results are presented to demonstrate the concentration polarization in the desalination module can significantly be alleviated by imprinting ribs over the surface of the membrane. These results are also aid in determining the coefficient of performance of modules containing ribs. The coefficient of performance is discussed in detail at the end of this section. It is clearly observed that concentration at membrane surface gradually increases as the flow hydrodynamically develops. It is also important to note that concentration over the surface of the membrane is uniform along the span-wise direction at all flow rates. It can be deduced from these results that flat sheet membranes are more prone to concentration polarization when compared against corrugated ones.

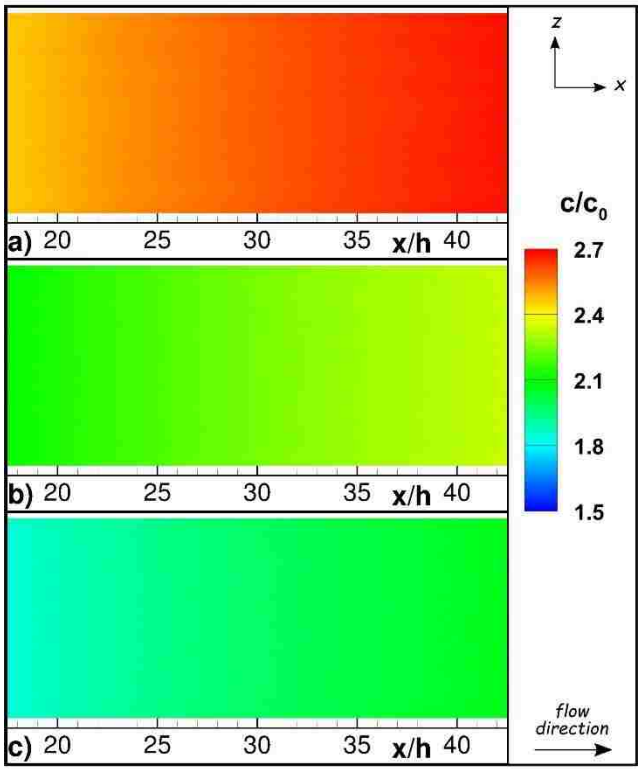

Figure 12. Contours of the concentration along the top membrane surface for empty channel. The normalized concentration contours are acquired at $Re = 100$ (a), $Re = 400$ (b) and $Re = 1000$ (c).

Sherwood number is calculated along the surface of the top membrane for $Re = 100$, 400 and 1000 in both geometry. Figure 13 depicts contours of Sherwood number along the membrane in desalination module with square and triangular ribs. Sherwood number in both module increases prominently with increasing flow rates. High Sherwood number regions correlate well with low polarization regions and high water flux regions along the surface of the membrane. This is very similar to the behavior observed in desalination modules containing mesh of spacers reported earlier by the present authors and other investigators [11,34,35].

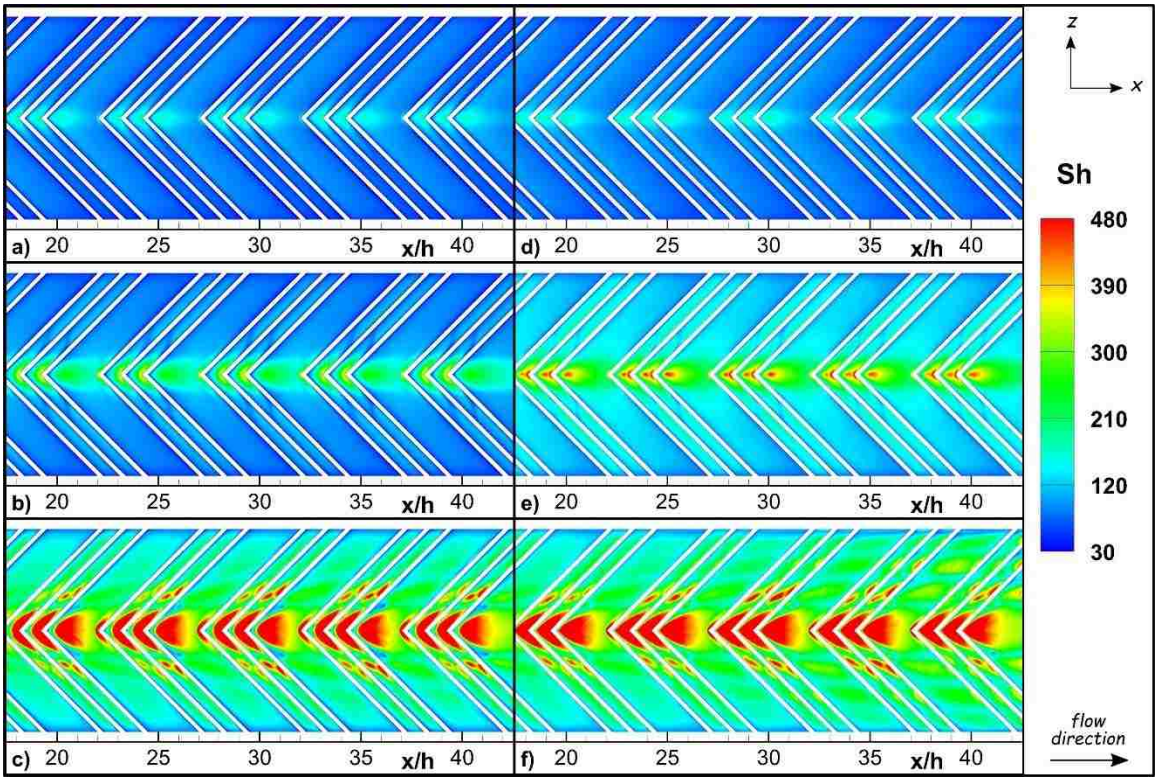

Figure 13. Contours of the local Sherwood number (Sh) along the top membrane surface for square ribs (left column) and triangular ribs (right column). The normalized local Sh contours are acquired at $Re = 100$ (a, d), $Re = 400$ (b, e) and $Re = 1000$ (c, f).

Wall shear stress is calculated along the surface of the top membrane in modules with square and triangular ribs. Contours of the skin friction are plotted in Fig. 14 for $Re = 100$, 400 and 1000 in both geometry. Bands of high shear regions along ribs follow regions of low concentrations. High shear regions are observed in the middle where ribs intersect at all flow rates. Wall shear stress distribution along the surface of the membrane also follows vorticity patters. It is reported that low shear regions along the surface of the membrane have higher probability of fouling occurrence [6,11,22,23]. Based on the prediction of wall shear stress in these modules fouling more likely occurs in small regions following ribs.

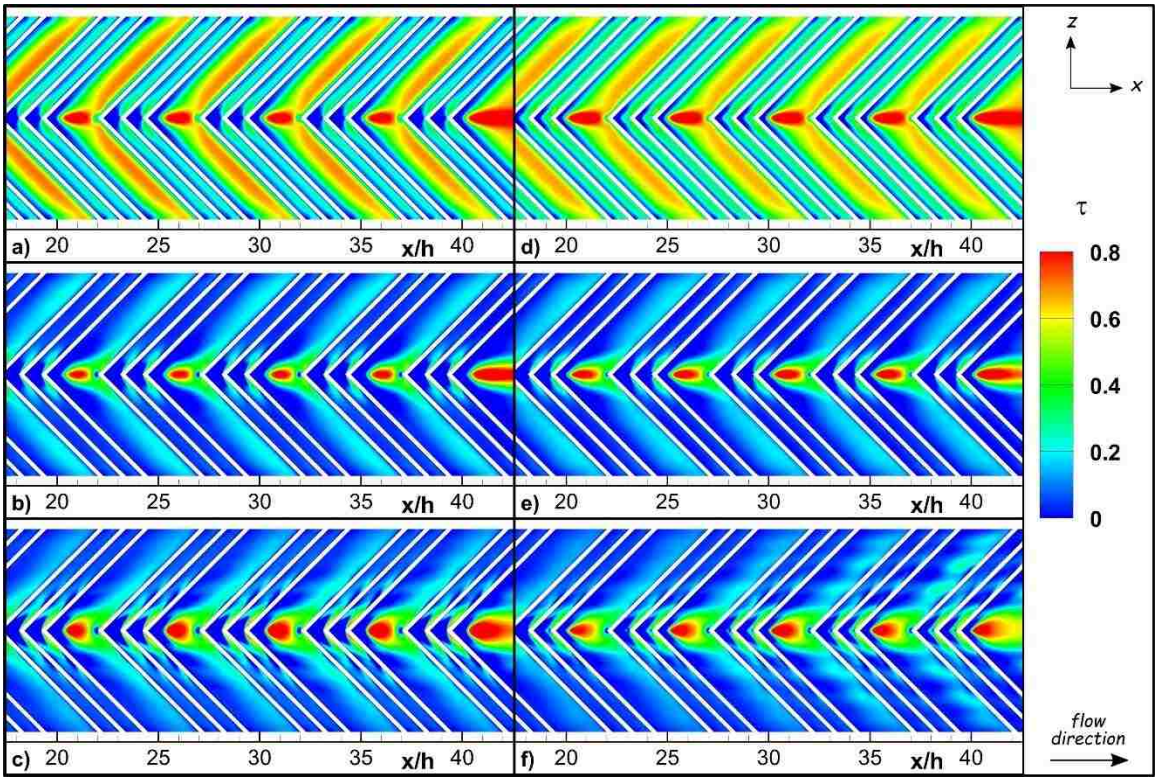

Figure 14. Contours of the wall shear stress (τ) along the top membrane surface for square ribs (left column) and triangular ribs (right column). The wall shear stress is normalized by maximum values acquired at $Re = 100$ (a, d), $Re = 400$ (b, e) and $Re = 1000$ (c, f).

To assess the performance of micromixers a merit criterion has to be introduced. Coefficient of performance (CP) determines the performance of membrane modules in comparison to a baseline case. The baseline is taken to be a module without ribs. Calculation of CP involves average Sherwood number and friction factor over a dedicated area for both improved and baseline case. In the current study the values are averaged over $25 \leq x/h \leq 40$ along the channel. Coefficient of performance is defined as

$$CP = \left(\frac{\overline{Sh}}{\overline{Sh}_s}\right)\left(\frac{f_s}{f}\right)^{1/3} \tag{11}$$

where $\overline{Sh}$ is the area averaged Sherwood number for geometry with ribs and $\overline{Sh}_s$ is the area average Sherwood number for geometry without ribs. f and f_s are the area averaged friction factor for geometries with and without ribs, respectively. Coefficient of performance, also referred as the merit number, measures membrane performance for the same pumping power. Table 2 shows calculated values of the average friction factor, Sherwood number and coefficient of performance for three values of Reynolds numbers. The friction factor decreases while Sherwood number increases as the flow speed increases, as depicted in Table 2. Since CP is greater in modules with both triangular and square ribs implementation of micromixers provide improved membrane performance at all flow rates. In particular, the merit number is tent to be higher for triangular ribs as they induce less friction while providing better momentum mixing that results in higher Sherwood number. It is also worth to mention that the coefficient of performance only measures performance based on mass transport quantities. Concentration polarization and fouling/scaling characteristics should also be considered to assess membrane performance. Even so, corrugation on the membrane surface induces the increased vortical activities and scouring that help to mitigation of concentration polarization and increasing the life-span of membranes.

Table 2. The average friction factor, the average Sherwood number and the coefficient of performance of all geometries at various flow rates

	Channel without ribs		Square ribs			Triangular ribs		
Re	f_s	$\overline{Sh}_s$	f	$\overline{Sh}$	CP	f	$\overline{Sh}$	CP
100	0.561	44.53	1.763	74.41	**1.167**	1.429	84.91	**1.428**
400	0.202	59.11	0.714	128.81	**1.432**	0.636	145.24	**1.678**
1000	0.089	74.88	0.617	220.13	**1.539**	0.603	247.34	**1.744**

This study focuses on steady-state flow and mass transport characteristics of the desalination module. It is recently documented by Anqi et al. [12,36] in a desalination module containing spacers there is a presence of strong transient three dimensional flows. Transient effects influence membrane performance immensely. Transient nature of flows in these systems can be attributed to flow separations. Thus a careful numerical study has to be devoted to investigate dynamics of flow and mass transports in these systems using high fidelity methods such as large eddy simulations.

5. Conclusion

Difficulties on understanding the mechanism of membrane separations due to the complexities inherit in membrane systems have always become a limiting factor for developing mathematical models while experimental studies were gradually illuminating the dark sides of actual transport mechanism. However recent developments on computational capabilities paved the ways of improved numerical models. Current study investigates the impact of membrane-based micromixers on mass transfer, concentration polarization by utilizing CFD simulations comprise the solution-diffusion model and SST k-ω turbulence model for Reynolds number up to 1000. The proposed model has been validated against an existing experimental study for the similar geometry. Qualitative and quantitative comparisons between predicted results and experimental measurements exhibit excellent agreement.

The validated model is implemented to predict flow and concentration phenomena in the proposed feed channel containing zigzagged square and triangular micromixers on the membrane surface. The results reveal that corrugations on membrane surface have significant influence on flow separation at all flow rates. As this separation occurs at near surface, disrupted boundary layers induce mitigation of high salt concentration and reduction of potential fouling at the membrane surface. Thus, vorticity sourced promoted mixing of low and high concentration fluid result in mass transfer enhancement. Further to that simulations for $Re = 1000$ indicates outstanding three-dimensional flow patterns that increase the wall shear stress, water permeation rate and induce scouring. Coefficient of

performance calculations suggest that triangular micromixers at Re of 1000 perform better compared to that square ribs.

References

[1] J.G. Wijmans, R.W. Baker, The solution-diffusion model: a review, J. Memb. Sci. 107 (1995) 1–21. doi:10.1016/0376-7388(95)00102-I.

[2] R.W. Baker, Membrane Technology and Applications, 3rd ed., John Wiley & Sons, Hoboken, 2012.

[3] S.S. Shenvi, A.M. Isloor, A.F. Ismail, A review on RO membrane technology: Developments and challenges, Desalination. 368 (2015) 10–26.

[4] G. Belfort, R.H. Davis, A.L. Zydney, The behavior of suspensions and macromolecular solutions in crossflow microfiltration, J. Memb. Sci. 96 (1994) 1–58.

[5] S.K. Karode, A. Kumar, Flow visualization through spacer filled channels by computational fluid dynamics I.: Pressure drop and shear rate calculations for flat sheet geometry, J. Memb. Sci. 193 (2001) 69–84.

[6] V. Geraldes, V. Semiao, M. Norberta de Pinho, Concentration polarisation and flow structure within nanofiltration spiral-wound modules with ladder-type spacers, Comput. Struct. 82 (2004) 1561–1568. doi:10.1016/j.compstruc.2004.03.052.

[7] G.A. Fimbres-Weihs, D.E. Wiley, Numerical study of mass transfer in three-dimensional spacer-filled narrow channels with steady flow, J. Memb. Sci. 306 (2007) 228–243.

[8] M. Shakaib, S.M.F. Hasani, M. Mahmood, CFD modeling for flow and mass transfer in spacer-obstructed membrane feed channels, J. Memb. Sci. 326 (2009) 270–284. doi:10.1016/j.memsci.2008.09.052.

[9] G. Srivathsan, E.M. Sparrow, J.M. Gorman, Reverse osmosis issues relating to pressure drop, mass transfer, turbulence, and unsteadiness, Desalination. 341 (2014) 83–86. doi:10.1016/j.desal.2014.02.021.

[10] A.E. Anqi, N. Alkhamis, A. Oztekin, Numerical simulation of brackish water desalination by a reverse osmosis membrane, Desalination. 369 (2015) 156–164. doi:10.1016/j.desal.2015.05.007.

[11] A.E. Anqi, N. Alkhamis, A. Oztekin, Computational study of desalination by reverse osmosis — Three-dimensional analyses, Desalination. 388 (2016) 38–49. doi:10.1016/j.desal.2016.03.017.

[12] A.E. Anqi, M. Alrehili, M. Usta, A. Oztekin, Numerical analysis of hollow fiber membranes for desalination, Desalination. 398 (2016) 39–51.

[13] C.P. Koutsou, S.G. Yiantsios, A.J. Karabelas, Membrane module performance optimization using CFD simulation of flow through narrow channels with spacers, in: Proc. IDA World Congr. Desalin. Water Reuse, 2007: pp. 21–26.

[14] C.P. Koutsou, S.G. Yiantsios, A.J. Karabelas, Direct numerical simulation of flow in spacer-filled channels: effect of spacer geometrical characteristics, J. Memb. Sci. 291 (2007) 53–69.

[15] P.R. Neal, H. Li, A.G. Fane, D.E. Wiley, The effect of filament orientation on critical flux and particle deposition in spacer-filled channels, J. Memb. Sci. 214 (2003) 165–178.

[16] A. Mahdavifar, A. Pollard, J.G. Pharoah, S.B. Beale, Wall proximity effects on flow over a simple membrane spacer, Comput. Fluids. 88 (2013) 180–188.

doi:10.1016/j.compfluid.2013.08.017.

[17] I.S. Kang, H.N. Chang, The effect of turbulence promoters on mass transfer—numerical analysis and flow visualization, Int. J. Heat Mass Transf. 25 (1982) 1167–1181.

[18] K. Scott, A.J. Mahmood, R.J. Jachuck, B. Hu, Intensified membrane filtration with corrugated membranes, J. Memb. Sci. 173 (2000) 1–16.

[19] S.H. Maruf, M. Rickman, L. Wang, J. Mersch IV, A.R. Greenberg, J. Pellegrino, et al., Influence of sub-micron surface patterns on the deposition of model proteins during active filtration, J. Memb. Sci. 444 (2013) 420–428.

[20] S.H. Maruf, A.R. Greenberg, J. Pellegrino, Y. Ding, Fabrication and characterization of a surface-patterned thin film composite membrane, J. Memb. Sci. 452 (2014) 11–19.

[21] J.A. Kharraz, M.R. Bilad, H.A. Arafat, Flux stabilization in membrane distillation desalination of seawater and brine using corrugated PVDF membranes, J. Memb. Sci. 495 (2015) 404–414.

[22] C.K. Ho, S.J. Altman, H.D.T. Jones, S.S. Khalsa, L.K. McGrath, P.G. Clem, Analysis of micromixers to reduce biofouling on reverse osmosis membranes, Environ. Prog. 27 (2008) 195–203.

[23] S.J. Altman, L.K. McGrath, H.D.T. Jones, A. Sanchez, R. Noek, P. Clem, et al., Systematic analysis of micromixers to minimize biofouling on reverse osmosis membranes, Water Res. 44 (2010) 3545–3554.

[24] A. Tamburini, M. Renda, A. Cipollina, G. Micale, M. Ciofalo, Investigation of heat

transfer in spacer-filled channels by experiments and direct numerical simulations, Int. J. Heat Mass Transf. 93 (2016) 1190–1205. doi:10.1016/j.ijheatmasstransfer.2015.11.034.

[25] F.R. Menter, Two-equation eddy-viscosity turbulence models for engineering applications, Am. Inst. Aeronaut. Astronaut. J. 32 (1994) 1598–1605. doi:10.2514/3.12149.

[26] L. Malaeb, G.M. Ayoub, Reverse osmosis technology for water treatment: State of the art review, Desalination. 267 (2011) 1–8. doi:10.1016/j.desal.2010.09.001.

[27] J. Wang, D.S. Dlamini, A.K. Mishra, M.T.M. Pendergast, M.C.Y. Wong, B.B. Mamba, et al., A critical review of transport through osmotic membranes, J. Memb. Sci. 454 (2014) 516–537. doi:10.1016/j.memsci.2013.12.034.

[28] M. Kargol, A. Kargol, Investigation of reverse osmosis on the basis of the Kedem–Katchalsky equations and mechanistic transport equations, Desalination. 190 (2006) 267–276.

[29] T. Okada, T. Matsuura, A new transport model for pervaporation, J. Memb. Sci. 59 (1991) 133–149.

[30] P. Sukitpaneenit, T.S. Chung, L.Y. Jiang, Modified pore-flow model for pervaporation mass transport in PVDF hollow fiber membranes for ethanol-water separation, J. Memb. Sci. 362 (2010) 393–406. doi:10.1016/j.memsci.2010.06.062.

[31] H.K. Lonsdale, U. Merten, R.L. Riley, Transport properties of cellulose acetate osmotic membranes, J. Appl. Polym. Sci. 9 (1965) 1341–1362.

[32] A.E. Anqi, N. Alkhamis, M. Alrehili, A. Oztekin, Numerical study of brackish water

desalination using reverse osmosis, Proc. IDA World Congr. Desalin. Water Reuse, San Diego, 2015. (2015). doi:10.13140/RG.2.1.4452.6565.

[33] A.E. Anqi, N. Alkhamis, M.F. Alrehili, A. Oztekin, Numerical study of brackish water desalination using reverse osmosis, in: Proc. IDA World Congr. Desalin. Water Reuse, San Diego, 2015.

[34] N. Alkhamis, D.E. Oztekin, A.E. Anqi, A. Alsaiari, A. Oztekin, Gas Separation Using a Membrane, ASME 2013 Int. Mech. Eng. Congr. Expo. Am. Soc. Mech. Eng. (2013) V07AT08A039-V007AT008A039. doi:10.1115/IMECE2014-37299.

[35] N. Alkhamis, A. Anqi, D.E. Oztekin, A. Alsaiari, A. Oztekin, Gas Separation Using a Membrane, in: American Society of Mechanical Engineers, 2014: p. IMECE2014-37299.

[36] A.E. Anqi, M. Usta, M. Alrehili, N. Alkhamis, A. Oztekin, Reverse Osmosis Desalination Module - Three Dimensional, Transient Analysis, ASME-IMECE2016. (2016).

Vita

Mustafa Usta was born in Beysehir, Turkey in 1988, the son of Meryem Usta and Nazım Usta. After completing his work at Selcuklu High School, he attended to the Yildiz Technical University in Istanbul where he received his Bachelor of Science in Mechanical Engineering in January 2012. Mustafa began pursuing his Master of Science in Mechanical Engineering at Lehigh University in 2013. During his graduate work, he started to study on computational fluid dynamics. During his time as a graduate student, Mustafa co-authored to number of publications.